

# Pore-Scale and Upscaled Investigations of Release and Transport of Lithium in Organic-Rich Shales

Jiahui You<sup>1</sup> · Kyung Jae Lee<sup>1</sup>

Received: 26 January 2023 / Accepted: 27 February 2024
© The Author(s), under exclusive licence to Springer Nature B.V. 2024

#### Abstract

To meet the extensive demand for lithium (Li) for rechargeable batteries, it is crucial to enhance Li production by diversifying its resources. Recent studies have found that produced water from shale reservoirs contains various organic and inorganic components, including a significant amount of Li. In this study, findings from hydrothermal reaction experiments were analyzed to fully understand the release of Li from organic-rich shale rock. Subsequently, numerical algorithms were developed for both pore-scale and continuum-scale models to simulate the long-term behavior of Li in shale brines. The experimental conditions considered four different hydrothermal solutions, including the solutions of KCl, MgCl<sub>2</sub>, CaCl<sub>2</sub>, and NaCl with various concentrations under the temperature of 130 °C, 165 °C, and 200 °C. The release of Li from shale rock into fluid was regarded as a chemical interaction of cation exchange between rock and fluid. The reactive transport pore-scale and upscaled continuum-scale models were developed by coupling the chemical reaction model of Li interaction between rock and fluid. The model was first implemented to investigate the release and transport of Li in the pore scale. Continuum-scale properties, such as effective diffusivity coefficients and Li release rate, were obtained as the fieldaveraged pore-scale modeling results. These properties were used as the input data for the upscaled continuum-scale simulation. The findings of this study are expected to provide new insight into the production of Li from shale brines by elucidating the release, fate, and transport of Li in subsurface formations.

**Keywords** Lithium resources  $\cdot$  Organic-rich shales  $\cdot$  Pore-scale modeling  $\cdot$  Rock-fluid interactions  $\cdot$  Fate and transport

#### **List of Symbols**

 $D_{\rm eff}$  Effective diffusion coefficient

 $D_i$  Molecular diffusivity of component i in fluid

k Local permeability

 $k_0$  Initial local permeability

Published online: 08 March 2024

 $R_i$  Reaction rate of component i in fluid

Department of Petroleum Engineering, University of Houston, 5000 Gulf Freeway, Houston, TX 77204, USA



 <sup>⊠</sup> Kyung Jae Lee kjlee6@central.uh.edu

- S Specific surface area
- $\varepsilon_{\rm f}$  Volume fraction of fluid area
- $\varepsilon_{\rm s}$  Volume fraction of rock
- $\overline{v}_{\rm f}$  Average velocity of fluid
- $\overline{p}_{\rm f}$  Average pressure
- $\mu_{\rm f}$  Dynamic viscosity
- $\rho_{\rm f}$  Fluid density
- $\rho_{\rm s}$  Rock density
- $\overline{\omega}_{f,i}$  Concentration of component i in fluid
- $\psi$  Diffuse-interface function

#### Subscripts

- f Fluid phase
- s Solid phase

## 1 Introduction

The demand for lithium (Li)-ion batteries has grown significantly with the increased usage of rechargeable energy storage for electronics, electrified transportation, and renewable electricity generation. According to the U.S. Geological Survey, 74% of Li consumption was for producing Li-ion batteries (USGS 2020). As such, the enhancement and diversification of the sources of Li supply are crucial for the successful clean energy transition. In general, Li is produced from solid minerals and brines in natural systems. Recent studies have found that produced water from shale reservoirs contained various organic and inorganic components, including an abundant amount of Li (Jang et al. 2017).

Currently, about two-thirds of Li supply is resourced from subsurface brines worldwide (Flexer et al. 2018). However, brines that contain high concentrations of Li are limited to the regions that extend between northwest Argentina, southwest Bolivia, and northern Chile (Flexer et al. 2018). This region is referred to as the Lithium Triangle, which could account for up to 80% of the world's Li brine resources. Li can also be extracted from solid minerals such as spodumene, petalite, and lepidolite. The cost of Li extraction from hard rock is known to be about twice of Li extraction cost from brines. Even though Australia ranks currently the number one in Li production from hard rock minerals worldwide (USGS 2020), it has been recently reported that the Li content in the produced water from Marcellus Shale could be about 230 ml/L (Phan et al. 2016), as shedding light on the potential diversification of the sources of Li supply.

Although shale brines have promising potential for Li supply, the current state-of-art lacks systematic knowledge relevant to the origin, fate, and transport of Li in shale brines (Lee 2022). Several researchers investigated Li originated from hydrocarbon source rocks and the subsequent evolution of formation water (Chan et al. 2002; Yu et al. 2013; Teichert et al. 2020). They found that depositional environments, thermal maturity of organic matter, and source rock age could influence Li isotopic compositions. The results suggest that  $\delta^7$ Li could be an efficient tracer to unravel the source of Li and track the accumulation location from the petroleum source rock system (Teichert et al. 2020). They provided strong evidence of Li evolution from the organic-rich source rocks. In the most recent study, Lee investigated the origin, fate, and transport of Li with a conceptual numerical model and found the location of Li accumulation in shale brines (Lee 2022). The release of



Li during the kerogen maturation in organic-rich source rocks and the subsequent process of fate and transport of released Li were considered during the numerical simulation. This basin-scale model study provided the knowledge of locating the high-concentration zones of Li in shale brines as a function of various geochemical factors.

This study aims to improve the prediction capability of the behavior of Li in organic-rich shale systems through pore-scale reactive transport modeling and upscaled continuum-scale modeling, with the reaction mechanisms of Li releasing from rock into fluid elucidated with experiments. To accomplish the objective of this study, we first analyzed the reaction kinetics of Li release from organic-rich shale rock obtained with hydrothermal reactions. Second, the reaction model was coupled with the pore-scale reactive transport models, to numerically describe the release and transport of Li. After developing the pore-scale reactive transport model, we applied it to both fracture-matrix and ideal grain models, considering the prevalence of the fracture-matrix system in reservoirs with natural fractures. Finally, we presented the upscaling method to describe the fate and transport of Li in the systems of organic-rich shales. The continuum-scale properties, such as effective diffusivity coefficients and Li release rate, were obtained as the field-averaged pore-scale modeling results with ideal grain models. The findings of this study are expected to provide a new insight into the production of Li from shale brines by elucidating the phenomena relevant to the release and transport of Li in subsurface formations.

## 2 Methodologies

## 2.1 Experimental Procedures

The experimental procedures and analysis of hydrothermal reactions have also been addressed with details in the work of the authors presenting a suite of geochemical experiments and characterizations of Li in shale rocks and brines (Lee et al. 2024). The hydrothermal reactions were conducted in the mechanical convection oven (Thermo Scientific Heratherm OMH60-S-SS) to elucidate the fluid–rock interactions resulting in the release of Li from the shale rock into the fluid. The hydrothermal liquids included deionized (DI) water and the solutions of KCl, MgCl<sub>2</sub>, CaCl<sub>2</sub>, and NaCl with various concentrations (0.01 M, 0.05 M, and 0.1 M). One-g-ground source rock powder from Green River Shale and 30-ml hydrothermal liquid were put into a high-pressure–high-temperature autoclave reactor with 50-ml-volume capacity. Each of the hydrothermal reaction experiments was continued for 72 h. The detailed conditions of hydrothermal reaction experiments are presented in Table S1 of Supplementary Information. After the reaction, the hydrothermal fluid was filtered and diluted for Inductively Coupled Plasma Mass Spectrometry (ICP–MS) analysis. We used ICAR RQ Thermo Fisher ICP–MS to perform the elemental analysis of Li.

We quantified the reaction kinetics of the release mechanisms of Li from shale rock into fluid, and the specific surface area of Green River Shale sample was analyzed with BET sorption analyzer. Anton Paar's NovaTouch was used with nitrogen as the adsorption gas. Detailed results of BET sorption analysis can be found in Table S2 of Supplementary Information.

Given that the release mechanism of Li in shale rock is known to be closely related to the kerogen maturity of shale, Rock-Eval analysis was conducted with Vinci RockEval-6 Pyrolysis Analyzer. The results of Rock-Eval pyrolysis analysis are provided in Table S3 of



Supplementary Information. The pyrolysis results confirmed that the Green River Shale contained Type I kerogen with low-marginal thermal maturity.

#### 2.2 Reaction Rate Law

The release mechanism of Li from shale rock into fluid was analyzed as the chemical reactions exchanging cations, given that the cation exchange has driven Li to be released from the source rock (organic-rich shale rock) during the hydrothermal reactions. The elucidated reaction kinetics were to be coupled with the mass-balance equation in the pore-scale modeling to account for the reactive transport of Li in shale systems. The chemical reaction model was established by measuring the Li concentration in hydrothermal fluids after the experiments. Given that KCl, MgCl<sub>2</sub>, CaCl<sub>2</sub>, and NaCl solutions were considered in this study, we have the following chemical reactions for the rock and fluid interactions that exchange cations:

$$Na^+ + Li - Shale(s) \rightarrow Li^+ + Na - Shale$$
 (1)

$$K^+ + Li - Shale(s) \rightarrow Li^+ + K - Shale$$
 (2)

$$Mg^{2+} + 2Li - Shale(s) \rightarrow 2Li^{+} + Mg - Shale$$
 (3)

$$Ca^{2+} + 2Li - Shale(s) \rightarrow 2Li^{+} + Ca - Shale$$
 (4)

We assumed that the reactions always occurred in the forward direction due to the low activity product, and thereby the chemical reaction rate was in a linear relationship with time. With the concentration of Na<sup>+</sup>, K<sup>+</sup>, Mg<sup>2+</sup>, Ca<sup>2+</sup>, and Li<sup>+</sup> ions measured before and after the reactions, the reaction rate could be obtained. The reaction rate of the exchanging cation (A) and shale rock can be described as the first order rate law, which has the following equations (Kimura et al. 1981):

$$A + bLi - shale(s) \rightarrow bLi^{+} + A - Shale$$
 (5)

$$-r_A = -\frac{1}{V}\frac{dN_A}{dt} = -\frac{1}{bV}\frac{dN_B}{dt} = ktSC_A t \tag{6}$$

where  $r_A$  is the reaction rate (mol/m<sup>3</sup> s);  $N_A$  and  $N_B$  are the numbers of moles of the cation (A) in solution and Li (B) in rock, respectively. kt is the reaction rate constant (m/s); S is the interfacial surface area (m<sup>2</sup>/m<sup>3</sup>);  $C_A t$  is the concentration of reacting cation (A) in solution; b is the chemical stoichiometry, which varies in different chemical reactions; b=1 when Na<sup>+</sup> and K<sup>+</sup> exchange with Li<sup>+</sup>, whereas b=2 when Ca<sup>2+</sup> and Mg<sup>2+</sup> exchange with Li<sup>+</sup>; and V is the volume of the particle (m<sup>3</sup>). In the pore-scale model, when we use mass-balance equation and apply the above reaction rate law in the source term, the chemical reaction rate has the following relationship:

$$-R_A = \gamma_A R_{\rm Li} \tag{7}$$

$$\gamma_A = \frac{V_{m,\text{Li}}}{bV_{m,A}} \tag{8}$$



where  $\gamma_A$  is stoichiometric coefficients based on molar mass and chemical valence, and  $V_{\rm m}$  is the molar volume (m³/mol), respectively.  $R_A$  and  $R_{\rm Li}$  are the reaction rate (kg/m³ s).  $V_{m,\rm Li}$  and  $V_{m,A}$  are molar volumes of Li and the cations (Na<sup>+</sup>, K<sup>+</sup>, Mg²<sup>+</sup>, and Ca²<sup>+</sup>), respectively. Calculated  $\gamma_A$  value for each chemical reaction was  $\gamma_{\rm Na} = 0.54$ ,  $\gamma_K = 0.28$ ,  $\gamma_{\rm Mg} = 1.84$ , and  $\gamma_{\rm Ca} = 0.997$ , respectively.

#### 2.3 Mathematical Method for Numerical Simulation

The governing equations of the developed pore-scale reactive transport model are listed in Table 1. The Darcy-Brinkmann-Stokes method (DBS) was implemented to solve the fluid flow and reactive transport in the pore-scale modeling. In the pore-scale model, the free zone and solid zone were denoted by the local volume fractions of pore  $(\varepsilon_f)$  and solid  $(\varepsilon_{\rm c})$  within the control volume. Here, the DBS momentum equation was used to describe the fluid flow in both fluid and solid zones. Where the last term  $(\mu_t k^{-1} \overline{\nu}_t)$  is the Darcy resistance term, which denotes the momentum exchange between the fluid and solid phase (You and Lee 2021b). In the fluid zone, the volume fraction of pore is 1, which makes the Darcy resistance term  $(\mu_f k^{-1} \overline{\nu}_f)$  zero, and the DBS momentum equation turns into the normal Navier-Stokes equation. Likewise, fluid flow in fracture zones is described with Navier-Stokes equation. In the solid zone, the volume fraction of the pore is near 0, and the Darcy resistance term becomes very large ( $\approx 10^{15}$  magnitude). This term in the solid zone can be regarded as a sink term, and the velocity becomes zero. Thus, the DBS method considers both the solid and fluid phases within a grid block at the fluid-rock interface. As such, unlike the traditional pore-scale modeling method, the stated DBS method includes the upscaled terms and effectively implements the non-slip boundary condition at the solid-fluid interface with the application of Darcy resistance term. The advection-diffusion mass-balance equations of the ions (Na<sup>+</sup>, K<sup>+</sup>, Mg<sup>2+</sup>, Ca<sup>2+</sup>, and Li<sup>+</sup>) were used to quantify the concentration of each ion in the fluid phase. Given that the weight loss of the source rock powder did not have an obvious change before and after the hydrothermal reaction experiments, we assumed that the local porosity of the rock did not change during the simulation.

The pore-scale reactive transport model was developed based on OpenFOAM, an open-source computational fluid dynamics (CFD) platform (Weller et al. 1998). This work was done by additionally describing the relevant physical-and-chemical phenomena in the source codes of pisoFOAM, which was initially designed to solve the incompressible transient flow (Leal 1992). The partial differential equations were discretized into linear algebraic equations by the finite volume method (FVM). The geometry models were generated by the open-source 3D computer graphics software, Blender (Blender Foundation

**Table 1** The governing equations of reactive transport modeling in pore–scale

Equation type	Main governing equation	Supplemental equations
Darcy–Brinkman–Stokes (DBS) momentum equation	$\frac{1}{\varepsilon_{\rm f}} \left( \frac{\partial \rho_{\rm f} \overline{v}_{\rm f}}{\partial t} + \nabla \cdot \left( \frac{\rho_{\rm f}}{\varepsilon_{\rm f}} \overline{v}_{\rm f} \overline{v}_{\rm f} \right) \right) = - \nabla \overline{p}_{\rm f} + \frac{\mu_{\rm f}}{\varepsilon_{\rm f}} \nabla^2 \overline{v}_{\rm f} - \mu_{\rm f} k^{-1} \overline{v}_{\rm f}$	$k^{-1} = k_0^{-1} \frac{(1 - \epsilon_t)^2}{\epsilon_t^3},$ $k_0 = 10^{-15} \text{ m}^2$
Advection-diffusion mass-balance equation	$\frac{\frac{\partial \varepsilon_{\rm f} \rho_{\rm f} \omega_{\rm f,i}}{\partial t} + \nabla \cdot \left( \overline{v}_{\rm f} \rho_{\rm f} \omega_{\rm f,i} \right) = \nabla \cdot \left( \varepsilon_{\rm f} \rho_{\rm f} D_i \nabla \omega_{\rm f,i} \right) - R_i(\omega_{\rm f,i}) , \label{eq:continuous_equation}$	$R_i = \rho_f k t S \omega_i t$ $S = \ \nabla \varepsilon\  \psi$ $\psi = 4\varepsilon_f (1 - \varepsilon_f)$



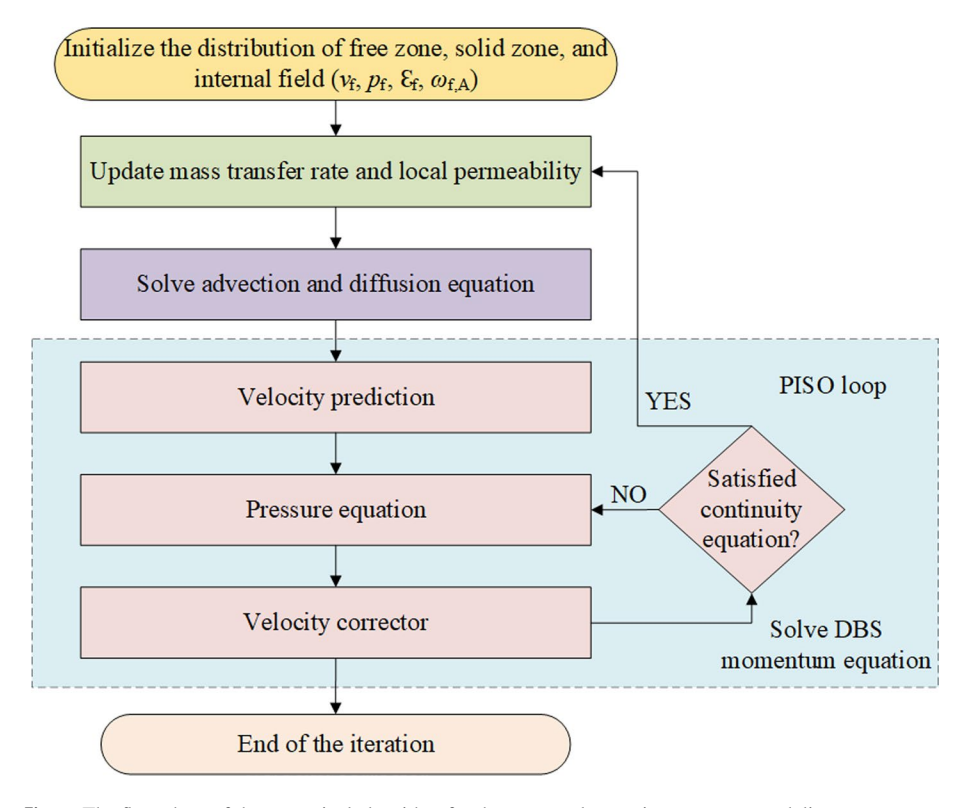


Fig. 1 The flow chart of the numerical algorithm for the pore-scale reactive transport modeling

**Table 2** The governing equations of reactive transport modeling in the continuum-scale model

Equation type	Main governing equation
Darcy's law Advection–diffusion mass-balance equa- tion	$U = -\frac{K}{\mu} \cdot (\nabla p - \rho g)$ $\frac{\partial \varphi \omega_{f,i}}{\partial t} + \nabla \cdot (U \omega_{f,i}) = \nabla \cdot (\varphi \tau D_{\text{eff}} \nabla \omega_{f,i}) - R$

1994). The initial volume fractions of the pores were initialized, and the initial and boundary conditions were set as follows:  $\bar{v}_f|_{t=0} = \bar{v}_{f0}$ ,  $\bar{v}_f|_{x=0} = \bar{v}_{f0}$ ,  $\frac{\partial \bar{p}_f}{\partial n}|_{x=0} = 0$ ,  $\bar{p}_f|_{x=x0} = \bar{p}_{out}$ ,  $\omega_{f,i}|_{x=0} = \omega_{f,i0}$ , and  $\omega_{f,i}|_{t=0} = 0$  (You and Lee 2021a, 2021b). The flow chart of the developed numerical algorithm is shown in Fig. 1.

The fluid flow and transport in the continuum-scale model was described by Darcy's Law and convention–diffusion equation. The equations are listed in Table 2. U and K are the velocity and permeability, respectively;  $\varphi$  is the porosity of the porous media;  $\tau$  is medium tortuosity, which equals to  $\varphi^{1/3}$ ;  $D_{\text{eff}}$  is the effective diffusivity coefficient; and R is the reaction rate of Li release. If the porous medium is considered as isotropic, K can be a scalar in the simulation. R and  $D_{\text{eff}}$  can be represented as the relationship with porosity and obtained from the pore-scale modeling.



The upscaling process for continuum-scale modeling with the results obtained with pore-scale modeling is shown in Fig. 2. We applied the developed pore-scale reactive transport model to calculate the Li concentration with respect to time and conducted the numerical tracer experiments over the synthetic ideal grain models. We obtained the reaction rate of Li being released from shale rock under different domain porosities. With numerical tracer experiments, the relationship between the effective diffusivity coefficients and porosity could be established. The relationships between reaction rate and effective diffusivity coefficient with respect to porosity were then obtained and used as the input data for the continuum-scale model. In the upscaled continuum-scale modeling, the fluid flow was described by the Darcy equation, and the transport of Li was described by the mass-balance equation, respectively. Porosity was used to denote the volume percentage of the void space of bulk rock, which had a range from 0 to 1. The continuum-scale geometry model had three geological layers as follows: the caprock layer at the top had a porosity of 0.1; the source rock layer and the brine accumulation layer were initialized with the random porosity fields, following the normal distributions with the mean of 0.4 and the standard deviation of 0.05. The source rock layer contained organic matter and minerals where solid Li was contained.

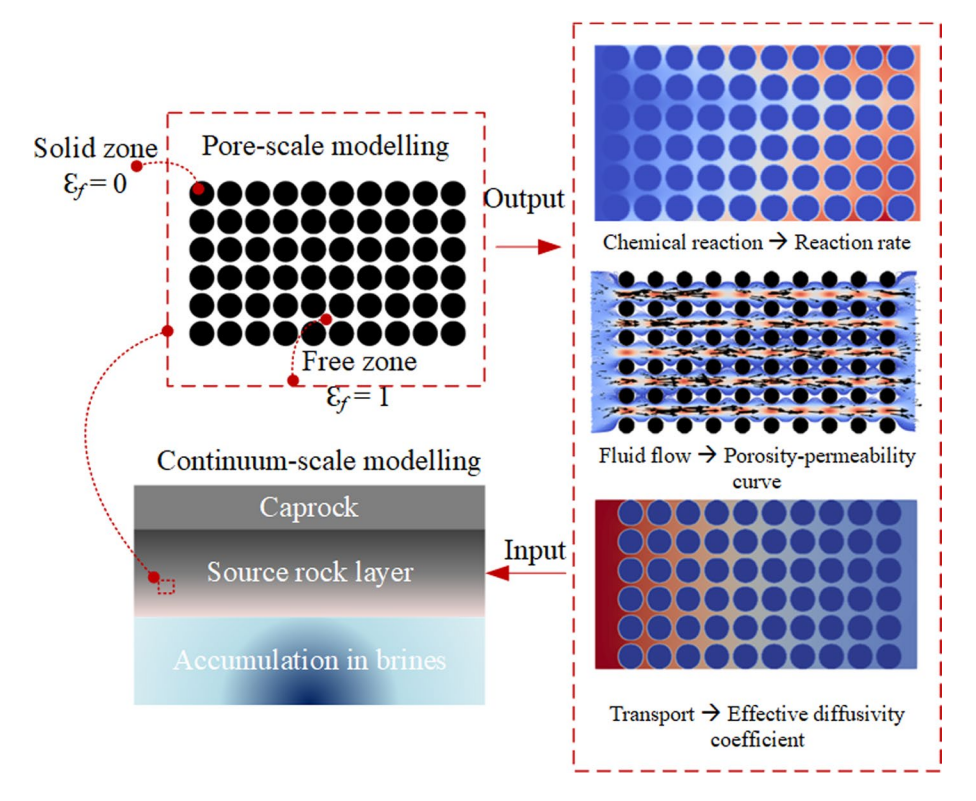


Fig. 2 The workflow of pore-scale reactive transport modeling and upscaled continuum-scale modeling

## 3 Results and Discussion

## 3.1 Hydrothermal Reaction Experiments

The ICP-MS results of Li concentration after the hydrothermal reactions for 72 h are summarized in Table S4 of Supplementary Information. As can be seen, the hydrothermal solution and its concentration had a significant influence on the Li release from shale rock into the fluid. At 130 °C and 165 °C, the temperature did not have a significant impact on the Li release. It is also observed that the different hydrothermal solutions had different sensitivity to the temperature of the Li release. CaCl<sub>2</sub> solution had the highest efficiency in releasing Li from shale rock into fluid, whereas the efficiency of cation exchange showed a relatively insignificant sensitivity to the temperature. With the hydrothermal temperature of 200 °C, the released Li concentration was generally higher than the cases of 130 °C and 165 °C. For most of the solutions, especially for KCl and MgCl<sub>2</sub>, released Li concentration in fluid showed values close to the cases of 130 °C and 165 °C-hydrothermal temperatures. The determined reaction rate constants for different hydrothermal solutions and temperatures are listed in Table 3. CaCl<sub>2</sub> solutions showed a relatively larger reaction rate constant than other solutions. This was because Ca<sup>2+</sup> had the fastest hydration shell exchange rate, which made it easier to exchange for bound Li (Eberl 1980a; Sawhney 1972a). In addition, it is also known that heavier element with higher ionic charge is easier to be fixated in the interlayer of clay under humid condition by exchanging with lighter element with lower ionic charge (Sawhney 1972b; Vine 1975; Eberl 1980b). Shale rock mainly contains organic compounds and various minerals such as clay, carbonate, and quartz, where Li is inorganically bound as an interlayer cation of clay in shale rock. Especially for Mg<sup>2+</sup> with the same ionic charge to Ca<sup>2+</sup>, the ion exchange capacity of Ca<sup>2+</sup> is much stronger than Mg<sup>2+</sup> on the surfaces of minerals or exchange sites in soils and clays due to its larger ionic radius (Chapman 1965).

**Table 3** Reaction rate constants for various systems

System	Temperature (°C)	Reaction rate constant (m/s)
Na-Li	130	$2.5858 \times 10^{-14}$
Mg–Li	130	$2.3063 \times 10^{-14}$
Ca–Li	130	$1.9251 \times 10^{-13}$
K–Li	130	$4.7084 \times 10^{-14}$
Na-Li	165	$2.6999 \times 10^{-14}$
Mg–Li	165	$1.3075 \times 10^{-14}$
Ca–Li	165	$1.9434 \times 10^{-13}$
K-Li	165	$4.8852 \times 10^{-14}$
Na-Li	200	$7.0237 \times 10^{-14}$
Mg–Li	200	$5.9508 \times 10^{-14}$
Ca–Li	200	$2.1347 \times 10^{-13}$
K–Li	200	$7.3713 \times 10^{-14}$



#### 3.2 Pore-Scale Simulation with a Fracture-Matrix Model

To provide the pore-scale insight of Li release from shale rock into fluid and the subsequent transport, we synthesized the pore-scale fracture-matrix geometry model, as shown in Fig. 3a. The model had a dimension of  $7.2 \text{ mm} \times 4.9 \text{ mm}$  with  $300 \times 300 \text{ rectangular}$  grids (i.e., grid size of  $0.024 \text{ mm} \times 0.016 \text{ mm}$ ). The regions in black and gray indicate the rock grain and the fluid zone, respectively. The boundary condition is shown in Fig. 3b. The brine containing the cations of Na<sup>+</sup>, Mg<sup>2+</sup>, Ca<sup>2+</sup>, and K<sup>+</sup> was injected from the left-hand side of the domain. The left boundary was set as velocity inlet, and the right boundary was set as pressure outlet, respectively. The input parameters for this simulation and the brine's ion contents are presented in the following Tables 4 and 5, respectively.

Figure 4a shows the Li transport with respect to time. Li was generated around the surface of the grain after being released from it and tended to accumulate in the free zone around the rock matrix. The fracture area showed a relatively higher fluid velocity, as

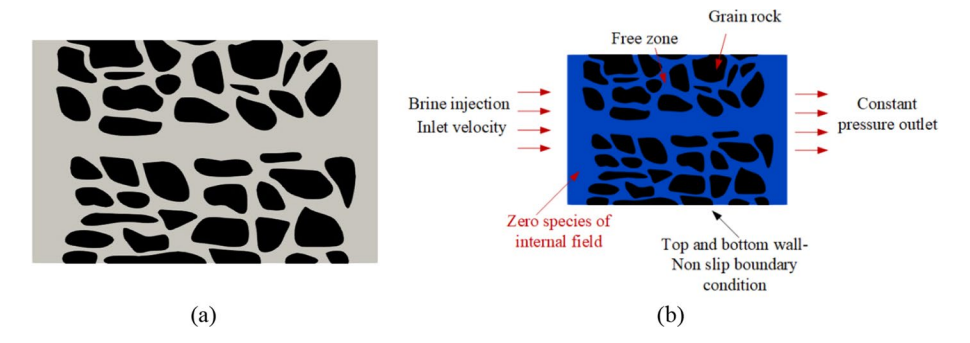


Fig. 3 a Geometry model of the pore-scale reactive transport simulation; b boundary conditions

**Table 4** The input parameters for the pore-scale modeling

Parameter	Value
Inlet velocity	$5 \times 10^{-6} \text{ m/s}$
Diffusivity coefficient of brine	$5 \times 10^{-9} \text{ m}^2/\text{s}$
Fluid density	$920 \text{ kg/m}^3$
Fluid viscosity	$2.4 \times 10^{-4} \text{ Pa s}$
System temperature	200 °C
Reaction rate constant of Na-Li system	$7.02373 \times 10^{-14}$ m/s
Reaction rate constant of Mg-Li system	$5.95078 \times 10^{-14}$ m/s
Reaction rate constant of Ca-Li system	$2.13457 \times 10^{-13}$ m/s
Reaction rate constant of K-Li system	$7.37131 \times 10^{-14}$ m/s

**Table 5** The cation compositions of injection fluid in the porescale modeling (Lee et al. 2024)

Cations in injected brine	Mass fraction (wt. %)
Na	3.09
K	0.064
Mg	0.3316
Ca	3.33



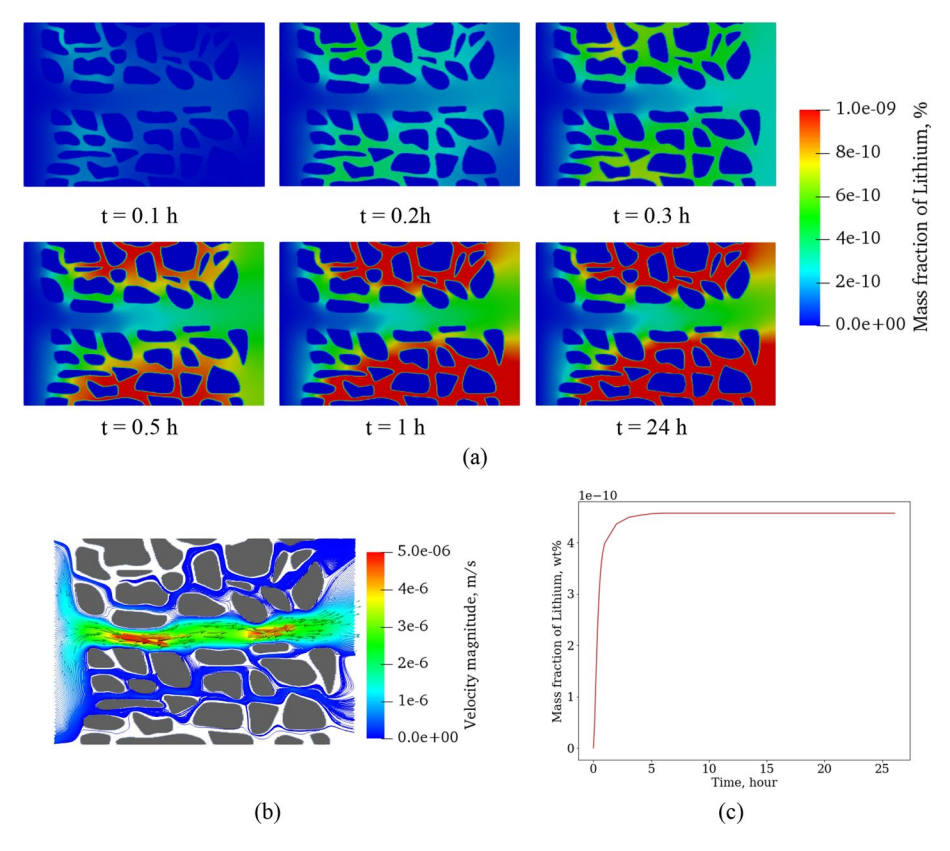


Fig. 4 a Li reactive transport in the fracture-matrix system with respect to time;  $\mathbf{b}$  streamlines and velocity magnitude of the fluid flow;  $\mathbf{c}$  average mass fraction of Li in the system with respect to time

shown in Fig. 4b. Figure 4b also presents the streamlines of the fluid flow, where the color of the streamline represents the magnitude of fluid velocity. Streamlines were distributed in the free zone around the matrix with a significantly low fluid velocity, which indicated that Li was easily accumulated in this area. As time passed, an abundant amount of Li was accumulated in the domain and approached the equilibrium. The average Li concentration in the computational domain with time is shown in Fig. 4c. Li concentration gradually reached the equilibrium state, where the average Li concentration in the system at the equilibrium was about  $10^{-10}$  wt%.

## 3.3 Pore-Scale Simulation with Ideal Grain Models

To systematically provide the pore-scale characteristics of Li release from shale rock into fluids by cation exchange and the subsequent transport, we generated homogeneously arranged ideal grain models with the porosity ranging from 0.26 to 0.73 (Fig. 5a) for pore-scale simulations. Given that the primary purpose of this work was to initiate discussions and provide a preliminary understanding of release of Li and its subsequent transport, we investigated the idealized conceptual models, to clearly understand the relevant phenomena in a general sense rather than in specific conditions with complex



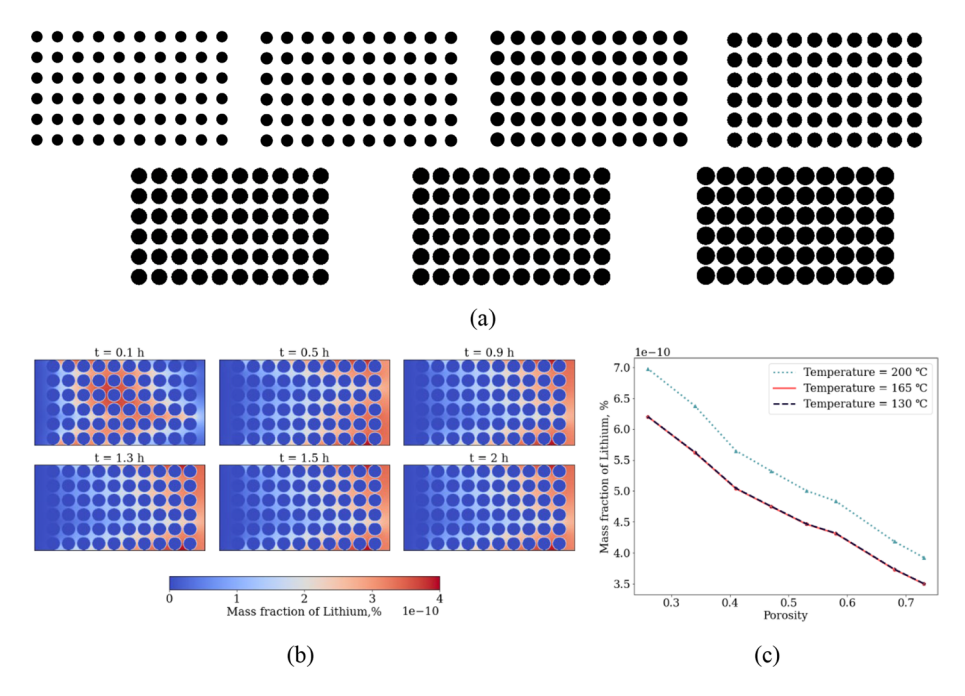


Fig. 5 a The schematics of the ideal grain models; **b** release and transport of Li at temperature = 165 °C and porosity = 0.34; **c** the average mass fraction of Li in the fluid under different conditions of porosity and temperature after the system reached the steady state (t=20 h)

mineral compositions and rock morphologies. The ideal grain models were integrated with upscaled models, to provide a prototype to study the release mechanisms of Li and estimate its accumulated quantity. It should be noted that while the ideal situation allows us to explore fundamental concepts, further research in more realistic environments in envisioned studies will be beneficial to validate and extend these findings to develop a large-scale model for future applications. The dimension of the computational domain was 9 mm × 4.45 mm with 360 × 250 rectangular grids (i.e., grid size of 0.025 mm × 0.018 mm), where the parameter setting was similar to the previous section. We mimicked the laboratory experiments of hydrothermal reactions to describe the Li release into fluid from the shale rock, which contained organic matter and minerals. As per the hydrothermal reaction experiments, we considered the reaction models at 130 °C, 165 °C, and 200 °C to simulate the process of Li release in the pore-scale ideal grain models. (The reaction rate constants with different experimental conditions are summarized in Table 3). We assumed that the grains contained abundant amount of Li as interlayer cations in a clay mineral. From the recent work of the authors, initial elemental concentration of Li in dried solid phase was about 0.0142 wt% in Green River Shale as obtained with ICP-MS analysis, and Li was mainly presented as Li<sup>+</sup> in bulk rock as obtained with Time-of-Flight Secondary-Ion Mass Spectrometry analysis (Lee et al. 2024). Figure 5b shows the Li release and transport at the beginning of the process. The top and bottom grains limited the flow at the boundary walls, and Li showed higher concentrations around the walls. We plotted the average mass fraction of Li concentration in the domain, when the domain reached the steady state. As stated in the



previous sections, at 130 °C and 165 °C, the cation exchange process was not sensitive to the system temperature (Fig. 5c). From the analysis of the thermogravimetric Analysis (TGA) and differential scanning calorimetry (DSC) of Green River Shale bulk rock in the authors' previous study (You and Lee 2022), it was observed that the significant weight loss of shale during the pyrolysis process occurred from the heating temperature of 200 °C, which was caused by the decomposing clay minerals and nahcolite (carbonate) minerals. As such, an active transformation of clay minerals explains the higher mass fraction of released Li at 200 °C case in Fig. 5c.

## 3.4 Upscaling for Continuum-Scale Modeling

To apply the findings from the laboratory experiments and pore-scale reactive transport modeling to the upscaled continuum-scale modeling, we first calculated the release rate of Li from shale rock into fluid and the effective diffusivity coefficient of Li in fluid with the results of ideal grain models presented in the previous section. The release rate of Li was obtained from the field-averaged Li concentration in fluid with respect to time. From the previous section of pore-scale simulation with the ideal grain models, we found that the concentration of Li in fluid rapidly reached equilibrium. The change of mass fraction of Li over the ideal grain models is shown in Fig. 6a. We could observe the turning point at about t=5 h. Before that, the brine flowed into the domain and accumulated. After t=5 h, the distribution of brine reached equilibrium, and the Li mass fraction presented the linear relationship with time. Thus, we assumed that the long-term Li release rate was under the brine's equilibrium. We then plotted the rate of Li (per unit volume) released into fluid with respect to porosity in Fig. 6c. This relationship between the release rate of Li with system porosity was included as a source term in the mass-balance equation of the upscaled continuum-scale modeling. In the continuum-scale model, the porous media are described by porosity, which represents the overall void volume relative to the total volume. In this section, concentration corresponds to the field average concentration over the control volume. (On the other hand, in the pore-scale model, concentration corresponded to each phase of fluid and solid.)

In the continuum-scale model, the effective diffusivity coefficient quantifies the overall diffusion behavior of the reactants within the porous media, considering both the diffusion within the material and the resistance imposed by its internal structures (El Oualid et al. 2017). Molecular movements are the driving force behind the effective diffusivity coefficient. In a pore-scale model, describing the diffusion phenomenon of fluid in the free zone is straightforward using the diffusion coefficient. Here, fluids can readily diffuse in the free zone but barely exhibit diffusion in the solid zone. To capture the same phenomenon in a continuum-scale model, it becomes necessary to identify the effective diffusivity coefficient under similar conditions. As the effective diffusivity coefficient is the important continuum-scale transport property, we calculated the effective diffusivity coefficient of the released Li in fluids, by matching the breakthrough curve of the numerical tracer experiment on the ideal grain pore-scale models and one-dimensional diffusion equation of the porous media (Deng et al. 2021). Here, the governing equation for the tracer experiment on the ideal grain pore-scale models is shown as follows:

$$\frac{\partial \varnothing C_{\text{tracer}}}{\partial t} = \nabla \cdot (\varnothing D \nabla C_{\text{tracer}}) \tag{9}$$



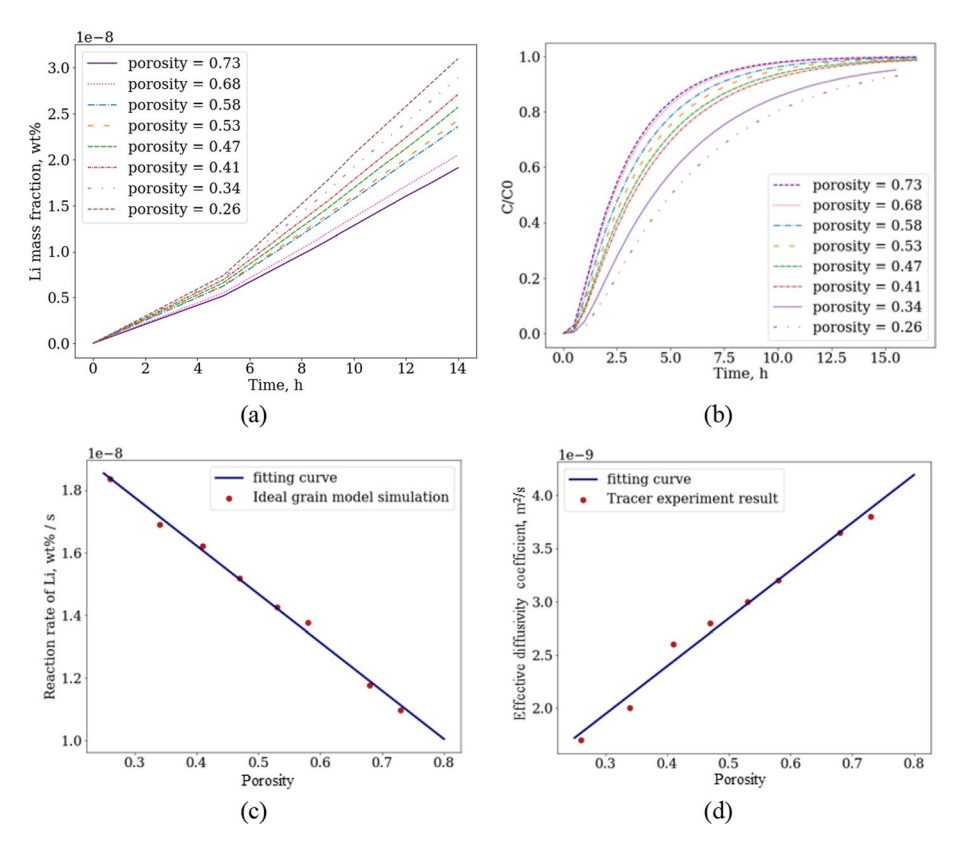


Fig. 6 a Changing Li mass fractions with time over the ideal grain models; **b** the normalized breakthrough curves of the numerical tracer experiment on the ideal grain pore-scale models, where  $C_0$  is the initial injection tracer concentration, and C is the concentration at outlet boundary, respectively; **c** the upscaled relationship between the rate of Li release from shale rock into fluid and porosity; **d** the relationship between the effective diffusivity coefficient of Li in fluid and porosity

The tracer experiment is used to measure the effective diffusivity coefficients for the porous media. In the above equation, D is the diffusion coefficient which equals to the molecular diffusion coefficient in the pore space of the pore-scale model (Deng et al. 2021). The diffusion of a solute in the continuum-scale model can be described by the following Fick's Law under the transient condition:

$$\frac{\partial C_{\text{tracer}}}{\partial t} = D_{\text{eff}} \frac{\partial^2 C_{\text{tracer}}}{\partial x^2}$$
 (10)

 $D_{\rm eff}$  is the effective diffusivity coefficient, which is relevant to the porosity and tortuosity of the porous media, where the tortuosity is the geometric parameter of pore space that cannot be measured directly. For the ideal grain pore-scale models, the non-reaction tracer with 1-M concentration was injected from left-hand side of the domain, while the right-hand side was set as a zero gradient boundary condition of concentration. Since the effective diffusivity coefficient represents the transport property of the discrete unit in porous media, the transport pattern is symmetric in Y-axis, and the diffusion of the tracer in porous media can be simplified to one dimension. Thus, we implemented the



one-dimensional diffusion simulation of the porous media using Fick's Law to find the corresponding effective diffusivity coefficient with the given geometrical structures.

The breakthrough curves on the pore-scale ideal grain models with different porosity values are plotted in Fig. 6b. After matching the breakthrough curves with the results of one-dimensional diffusion experiments, we could find the effective diffusivity coefficients for various porosities. The obtained effective diffusivity coefficients are summarized in Table 6. Between the porosity values of 0.26 and 0.73, the effective diffusivity coefficient showed a linear relationship with porosity (Fig. 6d). This was because the pore-scale ideal grain models were homogeneously generated with regular grain shapes. This relationship was included in the mass-balance equation of the upscaled continuum-scale modeling as well to track the transport phenomena of released Li in fluid.

We applied the derived upscaled reactive transport properties to the continuum-scale basin modeling, as shown in Fig. 7a. The model had a dimension of 9900 m in length and 5000 m in depth. The whole computational domain was discretized into 200×100 grids. The top layer of the caprock did not include Li in solid and fluid phases initially; the second layer of the source rock contained a high content of Li initially in solid phase (2 wt%), which was to be released into the fluid as rock and fluid interacted; the third layer of brine accumulation did not include Li in solid and fluid phases initially. The liquid phase existed in the pore volume under subsurface conditions, and the reaction time was much longer than in laboratory conditions. Thus, we considered 2 wt% of Li concentration as the inlet boundary condition to simulate the transported Li from nearby zone. In the pore-scale model, the inlet species contained the cations of Na<sup>+</sup>, Mg<sup>2+</sup>, Ca<sup>2+</sup>, and K<sup>+</sup> dissolved in water, with the concentrations indicated in Table 4. Following injection into the system, cation exchange occurred as leading to the release of Li from the rock. The averaged Li concentration was calculated from the pore-scale model and subsequently applied to the continuum-scale model for investigating the transport and long-term fate of Li. Thus, in the source rock layer, Li was originated from both newly released Li and transported Li from nearby zones. This simulation aimed to represent the conditions where Li has been accumulated from the source rock and subsequently transported and deposited over the long-term period. The source rock layer and the brine accumulation layer had random porosities, which followed the normal distributions with a mean of 0.4 and a standard deviation of 0.05. The left and right boundaries were set as fixed pressure boundary conditions. The input parameters are shown in Table 7. The Li release rate ranged between 1.34 and  $1.87 \times 10^{-8}$  wt%/s, and the effective diffusivity coefficient of Li ranged between 1.67 and  $3.2 \times 10^{-9}$  m<sup>2</sup>/s, as obtained

**Table 6** The effective diffusivity coefficients of Li under different porosities

Porosity	Effective diffusivity coefficients (m <sup>2</sup> /s)
0.73	$3.80 \times 10^{-9}$
0.68	$3.65 \times 10^{-9}$
0.58	$3.20 \times 10^{-9}$
0.53	$3.00 \times 10^{-9}$
0.47	$2.80 \times 10^{-9}$
0.41	$2.60 \times 10^{-9}$
0.34	$2.00 \times 10^{-9}$
0.26	$1.70 \times 10^{-9}$



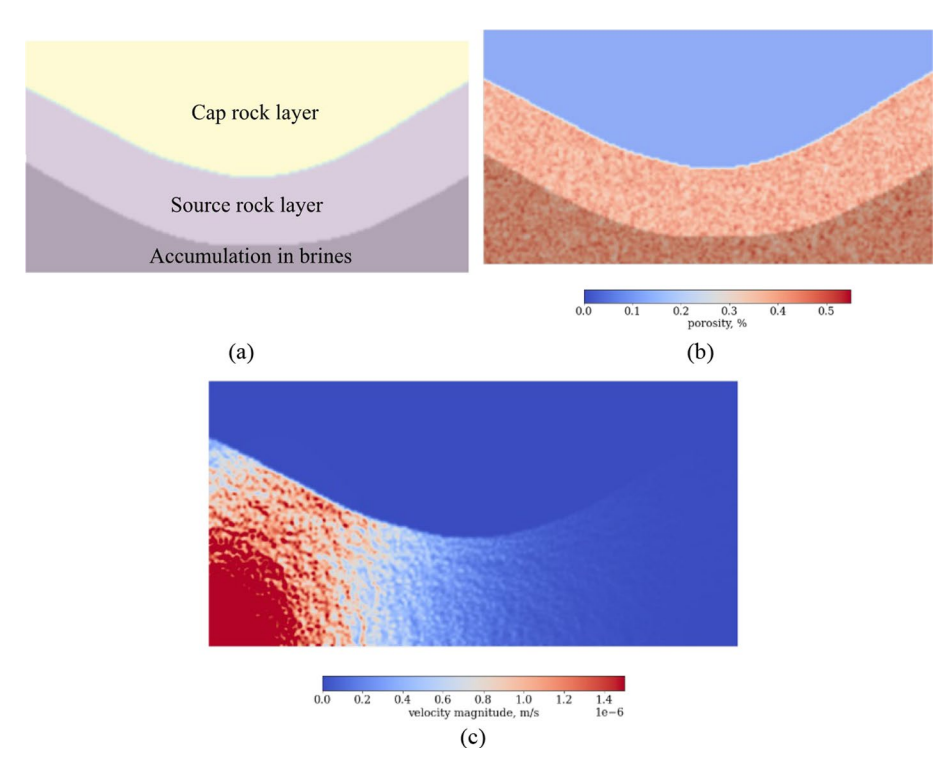


**Fig. 7** a The schematic of the continuum-scale geometry model; **b** the porosity distributions of three layers; **c** fluid velocity magnitude distribution in the field after 10 years

Table 7 Input parameters for the continuum-scale modeling

Parameters	Value
Inlet pressure	50 MPa
Outlet pressure	0 MPa
Inlet brine concentration	1.7 wt%
Porosity range of source rock layer and brine accumulation layers	0.24-0.58
Porosity of caprock layer $(\varphi)$	0.1
Relationship between the release rate of Li and porosity	$R_{\text{Li}} = 2.23 \times 10^{-8} - \phi \times 1.54 \times 10^{-8}$ (wt%/s)
Relationship between the effective diffusivity coefficient of Li and porosity	$D_{eff} = 4.5 \times 10^{-9} + \phi \times 5.9 \times 10^{-10}$ (m <sup>2</sup> /s)

with the upscaled results of pore-scale modeling. The pressure difference between the left and right boundaries was 50 MPa.

Figure 8 shows the transport of Li as a result of continuum-scale modeling. Initially, Li was mainly distributed in the pores of the source rock layer after being released from the rock. Given that Li is easily soluble in hydrous fluid (Williams et al. 2015), released Li was dissolved in fluid and transported through the pores. The hydrodynamic dispersion force drove the fluid containing Li from the left boundary to the center of the domain. While



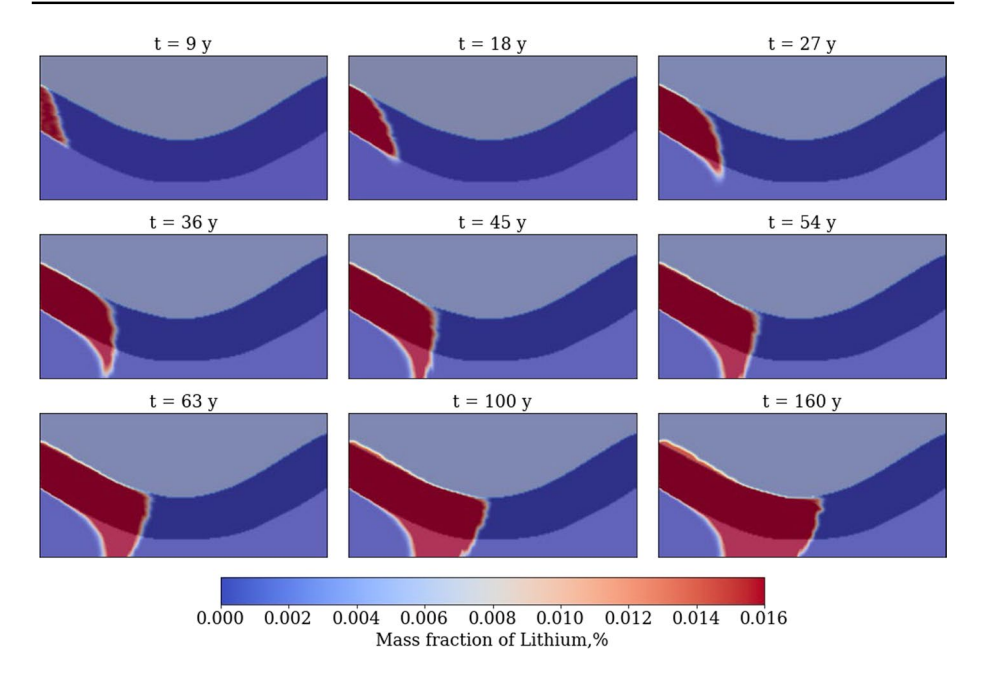


Fig. 8 The spatial distributions of mass fraction of Li in the continuum-scale model with respect to time

fluid flowed horizontally by the hydrodynamic dispersion force, fluid was under gravity force as well in the vertical direction with the hydrostatic pressure difference of 20 MPa between the top and bottom boundaries. Given that this continuum-scale model was established based on the thorough scientific findings from laboratory experiments and porescale modeling, it can reliably describe the release, transport, and long-term fate of Li, and hence provide critical insights on the potential locations of high concentration zones of Li in shale systems.

## 4 Conclusions

In order to meet the escalating demand of Li for renewable energy storage, it is critical to enhance Li production by diversifying its resources. In this study, we presented a comprehensive workflow involving laboratory experiments, pore-scale modeling, and upscaled continuum-scale modeling to reliably address the release of Li from shale rock into fluid, transport of Li through pores, and the fate of Li in the shale system. Where the reaction kinetics of Li releasing from rock into fluid were elucidated through the hydrothermal reaction experiments; release and transport properties of Li through pores were derived with pore-scale reactive transport modeling; long-term fate of Li in shale system was addressed by upscaled continuum-scale modeling. The findings of this study are expected to provide new insight into the production of Li from shale brines by thoroughly addressing the underlying subsurface phenomena.

**Supplementary Information** The online version contains supplementary material available at https://doi.org/10.1007/s11242-024-02071-2.



**Funding** The authors appreciate the funding for this research from National Science Foundation under Award 2042504 (CAREER: Identifying a New Source of Lithium for Sustainable and Renewable Energy Storage).

#### **Declarations**

**Conflict of interest** The authors declare no conflict of interests.

## References

- Blender Foundation, community. Blender. https://www.blender.org/.
- Chan, L.-H., Starinsky, A., Katz, A.: The behavior of lithium and its isotopes in oilfield brines: evidence from the Heletz–Kokhav field, Israel. Geochim. Cosmochim. Acta 66(4), 615–623 (2002)
- Chapman, H.D.: Cation-exchange capacity. In: Norman, A.G. (ed.) Methods of Soil Analysis: Part 2 Chemical and Microbiological Properties, pp. 891–901. American Society of Agronomy, Soil Science Society of America, Madison (1965)
- Deng, H., Tournassat, C., Molins, S., et al.: A pore-scale investigation of mineral precipitation driven diffusivity change at the column-scale. Water Resources Res. 57(5), e2020WR028483 (2021). https://doi.org/10.1029/2020WR028483
- Eberl, D.D.: Alkali cation selectivity and fixation by clay minerals. Clays Clay Miner. 28, 161-172 (1980a)
- El Oualid, S., Lachat, R., Candusso, D., et al.: Characterization process to measure the electrical contact resistance of gas diffusion layers under mechanical static compressive loads. Int. J. Hydrog. Energy 42(37), 23920–23931 (2017)
- Flexer, V., Baspineiro, C.F., Galli, C.I.: Lithium recovery from brines: a vital raw material for green energies with a potential environmental impact in its mining and processing. Sci. Total. Environ. **639**, 1188–1204 (2018)
- Jang, E., Jang, Y., Chung, E.: Lithium recovery from shale gas produced water using solvent extraction. Appl. Geochem. 78, 343–350 (2017)
- Kimura, S., Takagi, Y., Tone, S., et al.: A rate equation for gas-solid reactions accounting for the effect of solid structure and its application. J. Chem. Eng. Jpn. 14(6), 456–461 (1981)
- Leal, L.G.: Laminar Flow and Convective Transport Processes, vol. 251. Elsevier (1992)
- Lee, K.J.: Potential of petroleum source rock brines as a new source of lithium: insights from basin-scale modeling and local sensitivity analysis. Energy Rep. 8, 56–68 (2022)
- Lee, K.J., You, J., Gao, Y., et al.: Release, transport, and accumulation of lithium in shale brines. Fuel 356, 129629 (2024)
- Phan, T.T., Capo, R.C., Stewart, B.W., et al.: Factors controlling Li concentration and isotopic composition in formation waters and host rocks of Marcellus Shale, Appalachian Basin. Chem. Geol. 420, 162–179 (2016)
- Sawhney, B.L.: Selective sorption and fixation of cations by clay minerals: a review. Clays Clay Miner. 20, 93–100 (1972a)
- Teichert, Z., Bose, M., Williams, L.B.: Lithium isotope compositions of U.S. coals and source rocks: potential tracer of hydrocarbons. Chem. Geol. **549**, 119694 (2020)
- USGS. 2020. Lithium Data Sheet—Mineral Commodity Summaries 2020. https://pubs.usgs.gov/periodicals/mcs2020/mcs2020-lithium.pdf.
- Vine, J.D.: Lithium in sediments and brines—how, why, and where to search. J. Res. u. s. Geol. Surv. 3(4), 479–485 (1975)
- Weller, H.G., Tabor, G., Jasak, H., et al.: A tensorial approach to computational continuum mechanics using object-oriented techniques. Comput. Phys. 12(6), 620–631 (1998)
- Williams, L.B., Crawford Elliott, W., Hervig, R.L.: Tracing hydrocarbons in gas shale using lithium and boron isotopes: Denver Basin USA, Wattenberg gas field. Chem. Geol. 417, 404–413 (2015)
- You, J., Lee, K.J.: A pore-scale investigation of surface roughness on the evolution of natural fractures during acid dissolution using DBS method. J. Pet. Sci. Eng. 108728 (2021b). https://www.sciencedirect.com/science/article/pii/S0920410521003880
- You, J., Lee, K.J.: Pore-scale study to analyze the impacts of porous media heterogeneity on mineral dissolution and acid transport using Darcy–Brinkmann–Stokes method. Transp. Porous Med. 137(3), 575–602 (2021a)
- You, J., Lee, K.J.: The experimental investigation and data-driven modeling for thermal decomposition kinetics of Green River Shale. Fuel 320, 123899 (2022)



Yu, J.Q., Gao, C.L., Cheng, A.Y., et al.: Geomorphic, hydroclimatic and hydrothermal controls on the formation of lithium brine deposits in the Qaidam Basin, northern Tibetan Plateau, China. Ore Geol. Rev. 50, 171–183 (2013)

**Publisher's Note** Springer Nature remains neutral with regard to jurisdictional claims in published maps and institutional affiliations.

Springer Nature or its licensor (e.g. a society or other partner) holds exclusive rights to this article under a publishing agreement with the author(s) or other rightsholder(s); author self-archiving of the accepted manuscript version of this article is solely governed by the terms of such publishing agreement and applicable law.

